

Metallization of dense fluid helium from *ab initio* simulationsMartin Preising  and Ronald Redmer *Institut für Physik, Universität Rostock, D-18051 Rostock, Germany*

(Received 25 September 2020; accepted 4 December 2020; published 21 December 2020)

We examine the metallization of fluid helium with molecular dynamics simulations based on density functional theory. The insulator-to-metal transition is studied at densities between 1 and 22 g/cm³ and temperatures between 10 000 and 50 000 K. We calculate the equation of state, the band gap dependent on density and temperature by using different definitions, the DC conductivity, the reflectivity, and the ionization degree for which a novel method has been proposed recently [see M. Bethkenhagen *et al.*, *Phys. Rev. Research* **2**, 023260 (2020)]. We find no indication of a first-order phase transition in any of the properties studied here and therefore conclude that the metallization of fluid helium is continuous. For instance, we do not observe jumps in the DC conductivity and/or the reflectivity when the band gap closes. However, the ionization degree increases continuously from below 10% at the lowest to over 99% at the highest densities which reflects the continuous insulator-to-metal transition. The increase is almost exclusively driven by pressure ionization and shows only a weak temperature dependency. We discuss the high-pressure phase diagram of helium and the implications of our results on the structure of astrophysical objects like gas giant planets and brown dwarfs.

DOI: [10.1103/PhysRevB.102.224107](https://doi.org/10.1103/PhysRevB.102.224107)**I. INTRODUCTION**

Helium is generated by primordial nucleosynthesis in the early universe [1] or by hydrogen burning in stars [2]. After hydrogen, it is the second most abundant element and makes up about 23% of the baryon density in the universe. For a comprehensive understanding of many astrophysical processes the properties of hydrogen and helium have to be known for a wide range of densities and temperatures. Especially, this is the case for the formation and evolution as well as for the structure and composition of astrophysical objects like stars, brown dwarfs, and gas giant planets, where hydrogen and helium typically amount to about 98% of their mass. Of particular importance are the equation of state (EOS) data, optical properties like absorption, and the DC conductivity. The latter is a key input in dynamo simulations for the structure of the magnetic fields of these objects [3].

Therefore, the behavior of hydrogen and helium under extreme conditions has been in the focus of plasma, astro- and high-pressure physics for decades; for reviews, see Refs. [4–7]. Both hydrogen and helium are insulators at ambient conditions. The prediction of an insulator-to-metal transition (IMT) at high pressures, i.e., the *metallization* of molecular hydrogen and of atomic helium represents an intriguing problem in this context: How can their metallic-like electrical conductivities be traced back to their atomic properties? How do these change along the transformation pathway from ambient conditions to pressures of several megabar? These questions have inspired fundamental contributions to early quantum theory and solid state physics by, e.g., Herzfeld [8] and Mott [9]; for a review, see Ref. [10].

Wigner and Huntington [11] were the first to predict the transition from insulating molecular solid hydrogen to

metallic atomic solid hydrogen at 25 GPa at $T = 0$ K in 1935. Since then, enormous progress in understanding dense hydrogen has been made. Yet, the exact location of the IMT in the pressure-temperature diagram and the character of this transition is not precisely known, neither for the solid [6,12] nor the fluid domain [13–15]. A full understanding of the IMT in hydrogen still poses a great challenge, both for high-pressure experiments (e.g., measurement of temperature, interpretation of an increased reflectivity as signature for metallization) and *ab initio* simulations (e.g., treatment of nuclear quantum effects and of latent heat; see Ref. [16]). However, it is now consistently predicted to occur at few megabars (1 Mbar=100 GPa); see, e.g., Refs. [12,17] for recent surveys.

Consequently, the assumption that helium transforms to a metal upon sufficient compression has triggered many studies, although by far not as many as for hydrogen, see Refs. [18–21]. While the band gap (BG) of solid helium at zero temperature has been calculated with various approaches [22–25], ionization in dense helium plasmas has been treated within chemical models since the late 1980s [26–30]. Landau and Zeldovich [31] evaluated such ionization phenomena first. They concluded that the phase transition might be of first-order in a certain region of the phase diagram. This so-called *plasma phase transition (PPT)* would be connected with latent heat and a density jump between the two phases. Since then, a lot of effort has been made towards the prediction of the slope of the coexistence line of the PPT and the location of its critical point for hydrogen and other elements and compounds; see, e.g., Ref. [21]. Some of the models for helium predict two distinct phase transitions at high pressures: the first due to the ionization of neutral helium to He⁺, the second one due to a subsequent ionization of He⁺ to He²⁺. For instance, Förster *et al.* [26] locate the

critical point for the corresponding coexistence curve between the neutral and singly ionized fluids at around 35 000 K and 620 GPa (first PPT). They further predict a coexistence curve between the singly and twofold ionized fluids (second PPT) which ends in a second critical point at 114 000 K and 9 100 GPa.

Since the mid 2000s, the application of density functional theory (DFT) allowed for a more intricate description of the metallization transition in solid helium [32]. DFT coupled with classical molecular dynamics (MD) led to further investigations of the metallization transition of fluid helium in the physical picture [19,33–35]. Those studies could reach densities that are beyond the range of the most recent experiments on dense helium [20,36,37]. However, they did not exhibit any features of a thermodynamic instability, i.e., a PPT, that was predicted by chemical models as mentioned above.

In this study, we examine the metallization of fluid helium with DFT-MD and calculate the EOS, the DC conductivity, the reflectivity, and the ionization state for a broad range of densities (1–22) g/cm³ and temperatures (10 000–50 000) K. In particular, we study the evolution of the electronic BG and of the ionization degree as function of density and temperature. We search for jumps in the EOS, the DC conductivity, and the optical reflectivity, indicative of a first-order phase transition. The ionization degree is calculated with a novel method proposed recently [38]. Furthermore, we investigate whether or not metallic helium can exist at the extreme conditions in the interior of gas giant planets like Jupiter or in brown dwarfs like KOI 889b. We then discuss further implications of our results for astrophysics.

Our paper is organized as follows. In Sec. II, we introduce the computational methods for the EOS, the band gaps, the DC conductivity, the reflectivity, and the ionization degree. We then display and discuss the results in the same order in Sec. III, outline implications on the high-pressure phase diagram of helium and illustrate consequences for the behavior of dense helium in astrophysical objects.

II. METHODS

We apply a consistent approach for the calculation of the thermophysical properties of dense helium by treating the electrons with DFT [39,40] and combining this quantum-statistical description with classical MD for the ions. We employ the plane wave code VASP (*Vienna ab initio simulation package*) [41–45], in which the electronic bands are occupied according to Fermi-Dirac statistics. We adjust the number of bands as well as the size of the time step for each density and temperature under consideration in the same way as documented in Preising *et al.* [46]. We control the temperature of the ions with a Nosé-Hoover thermostat [47–49] and sample the Brillouin zone with different \mathbf{k} -point sets: the Γ point, the Baldereschi Mean Value Point (BMVP) [50], or a more elaborate Monkhorst-Pack set [51]. We use the Perdew-Burke-Ernzerhof (PBE) exchange-correlation (XC) functional [52] and employ pseudopotentials in the plane augmented wave (PAW) description [53] as well as the full Coulomb potential where necessary. The PAW pseudopotentials both treat two valence electrons. The difference between

the standard PAW and the hard PAW potential is the distance at which the augmentation of the wavefunction begins; it is smaller for the hard PAW (0.6 Å) than for the standard PAW (1.1 Å). Most important for the determination of precise thermophysical properties are careful checks of the convergence of the DFT-MD simulations; details are outlined in Ref. [54].

A. EOS

The pressure and internal energy are evaluated from DFT-MD runs after they have achieved thermodynamic equilibrium. We ensure that the total simulation time is at least 5 ps at every density and temperature grid point in this study.

B. Band gaps

It is known that DFT-based methods underestimate the band gap systematically depending on the number of atoms and the XC functional [30,34,35,55]. Nevertheless, we can gain valuable insight in the evolution of the BG dependency on density and temperature.

We examine and compare different definitions of the BG that were used in recent work on the behavior of dense helium, namely the *HOMO-LUMO* definition [33,35], the *broadened* method [34], and the *histogram* technique [32]. The latter is from our perspective best suited to identify the BG. Details of these methods are outlined in Ref. [54] (see, also, Refs. [26,27 and 32] therein).

C. DC conductivity

The dynamic electrical conductivity is calculated with the Kubo-Greenwood formula [56–60]:

$$\sigma^{\text{tot}}(\omega) = \frac{2\pi e^2}{3\omega\Omega} \sum_{\mathbf{k}} W(\mathbf{k}) \sum_{j=1}^N \sum_{i=1}^N \sum_{\alpha=1}^3 [F(\epsilon_{i,\mathbf{k}}) - F(\epsilon_{j,\mathbf{k}})] \times |\langle \Psi_{j,\mathbf{k}} | \mathbf{v} | \Psi_{i,\mathbf{k}} \rangle|^2 \delta(\epsilon_{j,\mathbf{k}} - \epsilon_{i,\mathbf{k}} - \hbar\omega). \quad (1)$$

Here, the Fermi-Dirac occupation $F(\epsilon_{i,\mathbf{k}})$ of the i th band that corresponds to the energy $\epsilon_{i,\mathbf{k}}$ and the wave function $\Psi_{i,\mathbf{k}}$ at \mathbf{k} -point \mathbf{k} is summed up over the spatial directions α and the bands i and j . The prefactor contains the electron charge e , the frequency ω , and the supercell volume Ω .

The DC conductivity is the low-frequency limit of the dynamic electrical conductivity:

$$\sigma_{\text{DC}} = \lim_{\omega \rightarrow 0} \sigma^{\text{tot}}(\omega). \quad (2)$$

D. Reflectivity

We calculate the reflectivity R at 532 nm as in Preising *et al.* [46] via the Fresnel formula,

$$R(\omega) = \frac{[n_0(\omega) - n(\omega)]^2 + [k_0(\omega) - k(\omega)]^2}{[n_0(\omega) + n(\omega)]^2 + [k_0(\omega) + k(\omega)]^2}, \quad (3)$$

with the complex index of refraction, $n + ik$. The subscript 0 denotes the material at the reflecting boundary. The complex index of refraction results from the complex dielectric

function $\varepsilon(\omega) = \varepsilon_1(\omega) + i\varepsilon_2(\omega)$ as

$$n(\omega) + ik(\omega) = \sqrt{\varepsilon(\omega)}, \quad (4)$$

$$\varepsilon_1(\omega) = \frac{\sigma_2(\omega)}{\varepsilon_0\omega}, \quad (5)$$

$$\varepsilon_2(\omega) = 1 - \frac{\sigma_1(\omega)}{\varepsilon_0\omega}. \quad (6)$$

Here, we obtain the real part of the dynamic conductivity $\sigma_1(\omega)$ from the Kubo-Greenwood formula (1) and calculate the imaginary part $\sigma_2(\omega)$ from $\sigma_1(\omega)$ with a Kramers-Kronig relation; see Refs. [58,60–63] for further details. The testing regime for the optical reflectivity at 532 nm was identical with that of the DC conductivity.

E. Ionization

Bethkenhagen *et al.* [38] proposed a new method to calculate the ionization degree of high-density plasmas via the dynamic electrical conductivity obtained from DFT-MD simulations and an evaluation of the Kubo-Greenwood formula, Eq. (1). Former work instead relied on the DOS to analyze the ionization degree [64–66]. We provide a brief summary of the approach; for details, see Refs. [38,54].

The dynamic electrical conductivity has to satisfy the Thomas-Reiche-Kuhn (TRK) sum rule [67–70],

$$Z^{\text{tot}} = \frac{N_e^{\text{tot}}}{N_i} = \frac{2m\Omega}{\pi e^2 N_i} \int_0^\infty d\omega \sigma^{\text{tot}}(\omega), \quad (7)$$

with the total charge state Z^{tot} , the total number of electrons N_e^{tot} and ions N_i , and the dynamic electrical conductivity $\sigma^{\text{tot}}(\omega)$. For helium, Eq. (7) is fulfilled if $Z^{\text{tot}} = 2$. We then partition the TRK sum rule into different electronic contributions and calculate the ionization state α from the number of electrons of each contribution as

$$\alpha = \frac{Z^{\text{c-c}}}{Z^{\text{tot}}}, \quad (8)$$

where $Z^{\text{c-c}}$ is the effective number of electrons per ion that contributes to electronic transition within the conduction band.

III. RESULTS

If the IMT of helium is a first-order phase transition we should observe discontinuities in the thermodynamic functions due to latent heat. The IMT should then be accompanied by BG closure and abrupt changes (jumps) of the DC conductivity, the reflectivity, and the ionization degree. Similar studies on the metallization in dense fluid hydrogen have shown that the discontinuities are generally more pronounced at lower temperatures [71–73].

In order to constrain our study to the fluid regime we only consider temperatures starting from 10 000 K and densities below the corresponding melting density of (21.3 ± 0.7) g/cm³; see Ref. [74].

A. EOS

We calculate pressures P and internal energies u for given densities ρ and temperatures T from the DFT-MD runs. In

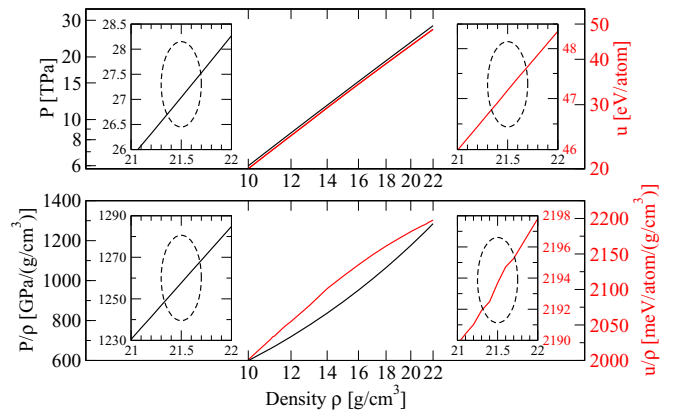


FIG. 1. (Top) Pressure P (black, left y axis) and internal energy per atom u (red, right y axis) for fluid helium at 10 000 K as function of density ρ . (Bottom) P/ρ (black, left y axis) and u/ρ (red, right y axis). The insets depict P and u over the density range where the BG closes according to the *histogram* method. The density range of interest is further highlighted by dashed ellipses.

case of a first-order phase transition, we should observe a plateau in P (density jump) and a jump in u (latent heat). The upper panel of Fig. 1 displays the pressure P and internal energy u at the lowest temperature considered here, i.e., 10 000 K. In order to illuminate the influence of correlation effects which should change considerably at the IMT, we show P/ρ and u/ρ in the lower panel. The insets left and right zoom into the density region where metallization occurs.

We do not observe a plateau-like structure in P or a jump in u in the entire density range but find some faint features in the raw data of u/ρ in the density range where the BG closes according to the *histogram* approach. However, the statistical fluctuations of u/ρ under these conditions are larger than ± 4 eV/atom/(g/cm³) in our MD runs. We therefore conclude that no noticeable behavior of P , u , P/ρ , and u/ρ occurs when the BG closes in fluid helium at 10 000 K. Furthermore, we do not find any features at higher temperatures or at densities where the BG closes according to the *broadened* method.

B. Band gaps

In order to determine the location of the band gap closure, we calculate isotherms at $T_x = 10^x$ with $x=4, 4.1, \dots, 4.7$ at a density grid of 1 g/cm³ width. By progressively decreasing the density interval we iteratively find the density at which the BG closes within 0.1 g/cm³ according to the *histogram* and *broadened* method. We then compare our results for the BG with values from Refs. [33–35] in Fig. 2.

While we reproduce the results of the *broadened* method of Ref. [34] at 20 000 K, we obtain different results at higher and lower temperatures. The reason for this discrepancy is most likely due to the use of a different XC functional. While Ref. [34] performed the DFT-MD simulations with the PBE [52] XC functional, they then determined the BGs using snapshots and the PW91 [75] XC functional. We performed all calculations with the PBE XC functional and used data from MDs to calculate the BG.

Our results reproduce the *HOMO-LUMO* results of Refs. [33,35] for all conditions of our study within the error

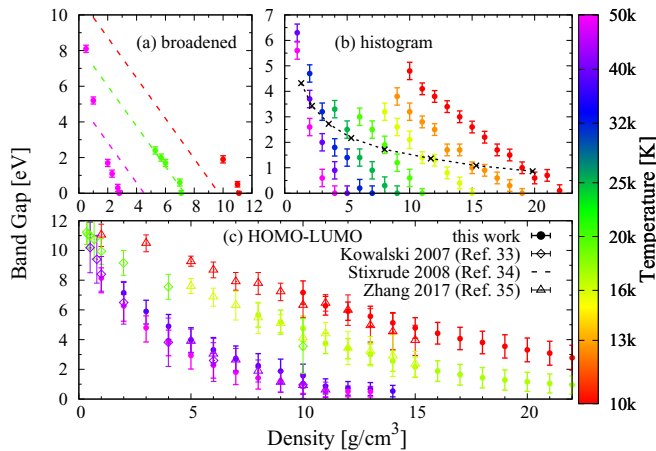


FIG. 2. Evolution of the BG with density for a set of isotherms (color-coded). Results of this work are always depicted as closed circles. (a) on the upper left shows the results of the *broadened* method of Ref. [34] as dashed lines as well as the *broadened* results of this work. (b) on the upper right displays the results of the *histogram* approach of this work. The dashed line represents the conditions where the BG is equal to $k_B T$. (c) compares results of this work with those of Refs. [33,35] within the *HOMO-LUMO* approach to the BG as open diamonds and upper triangles, respectively.

bars. However, as we discuss in Ref. [54], we could not obtain converged results with the snapshot-based methods of Refs. [33,35], even with a greater number of atoms and better \mathbf{k} -point sampling. Essentially, the BG results with the *HOMO-LUMO* method can be shifted by an arbitrary energy offset, depending on the chosen number of atoms, see Fig. S4 in Ref. [54]. Our calculations show that converged BGs in dense helium can only be obtained via MD simulations and by using the *histogram* or *broadened* technique, see Ref. [54].

C. DC conductivity

The DC conductivity σ_{DC} has been calculated from the Kubo-Greenwood formula, Eq. (1), for every isotherm and at least five corresponding densities. We increased the number of density points at lower temperatures, see Fig. 3. For the determination of σ_{DC} , we averaged over up to 20 ionic snapshots of the MD simulations; see Ref. [54] for further details. Due to the results of Sec. III B, we know the densities at which the BG closes according to the *histogram* method, see Fig. 2. If necessary, we interpolate σ_{DC} between the two most close-lying points and include this interpolated DC conductivity at conditions where the BG closes in Fig. 3. In a similar fashion, we interpolate the density where $k_B T$ is identical to the BG for every isotherm. We then interpolate the σ_{DC} at these densities in order to study whether the slope of the band gap over density changes when $k_B T$ approaches the BG. Additionally, we compare to the minimum metallic Mott conductivity $\sigma_{Mott} = 0.2 \times 10^6$ S/m and to values given in Refs. [33–35,55].

At the lowest temperatures, we observe a strong increase of the DC conductivity with the density that tends to become more flattened out at densities above the BG closure, i.e., in the metallic region. We do not see this feature in the results of

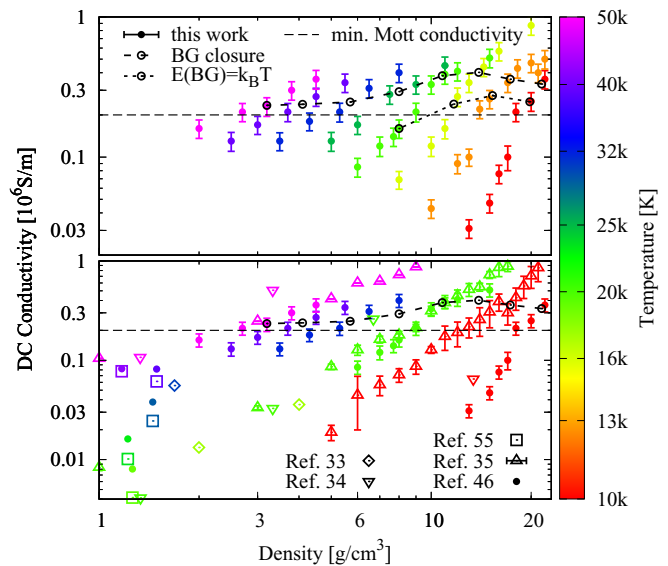


FIG. 3. DC conductivity as a function of density for different isotherms (color-coded). The upper panel shows the results of this work as filled circles. Open black symbols along the dashed line denote the interpolated DC conductivity at conditions where the BG closes according to the *histogram* method. Open black symbols along the dotted line denote the interpolated DC conductivity at conditions where the BG equals the thermal energy $k_B T$, see Fig. 2(b). The thin dashed line represents the minimum Mott conductivity at $T = 0$ K [10]. The lower panel compares our results (filled circles) for selected isotherms with the results of Kowalski *et al.* [33], Stixrude *et al.* [34], Soubiran *et al.* [55], Zhang *et al.* [35], and Preising *et al.* [46] that are denoted as open diamonds, lower triangles, squares, upper triangles, and filled circles without error bars, respectively.

Ref. [35]. The strong increase with density does not correlate strongly with the BG closure. Instead, it more strongly correlates with the conditions where the thermal energy approaches the value of the BG and the minimum Mott conductivity of 0.2×10^6 S/m given in Ref. [10]. This indicates that thermal excitations in this region lower the electronic resistance significantly and therefore increase the conductivity. Furthermore, the increase of the DC conductivity becomes less pronounced with increasing temperature due to these thermal effects. Note that the behavior of the DC conductivity of dense fluid helium as a function of density and temperature is very similar to earlier results for the continuous nonmetal-to-metal transition observed in expanded fluid metals [76,77] and noble gases [78,79].

We do not see jumps of the electrical conductivity in any of the isotherms, contrary to the results obtained for the metallization of dense fluid hydrogen [71,72]. In conjunction with the results for the EOS shown in Fig. 1 this clearly indicates that the metallization of dense fluid helium is a continuous transition of higher order.

While we reproduce the results of Ref. [35] at higher temperatures within the error bars, the strong increase of our DC conductivity at 10 000 K occurs at higher densities compared to Ref. [35]. This is likely due to the different implementations and codes used in Ref. [35] and in this study. At low

temperatures, the results of Ref. [35] seem to exhibit a similar change of slope around the minimum Mott conductivity, although the change is not as pronounced compared to our results. The low-density trends of our results reproduce all the available literature values to the best of our knowledge. At higher densities where no experimental results are available to date, we concur with the results of Ref. [33]. The high-density results of Ref. [34] are shifted toward higher DC conductivities compared to our results and those of Ref. [35]. We attribute this difference to the use of different XC functionals and finize size effects. Reference [35] employed the PW91 XC functional and 64 atoms, we used PBE and at least 128 atoms.

The DC conductivity at which the BG closes according to the *histogram* method (0.2–0.6 MS/m, see Fig. 3) is smaller than the DC conductivity at which the BG closes according to the *HOMO-LUMO* definition in Ref. [35] (0.7–1.0 MS/m). This trend is reasonable considering the differences of the results obtained for the *HOMO-LUMO* and the *histogram* approach displayed in Fig. 2 as well as in Fig. S4 of Ref. [54]. We emphasize again in this context that the BG of the *HOMO-LUMO* technique cannot be converged with respect to the number of atoms; see Ref. [54].

D. Reflectivity

We calculate the optical reflectivity at 532 nm for every isotherm at the same densities as in Sec. III C and perform the same interpolations as we did for the DC conductivity shown in Fig. 3. In a previous study [46], we calculated the reflectivity with different XC functionals under the conditions reported in Ref. [80]. We compare our results to Refs. [33,35,80], and the results of the PBE XC functional of Ref. [46], see Fig. 4.

Similar to the results for the DC conductivity (Fig. 3), we obtain a strong increase of the reflectivity with the density at the lowest temperatures that tends to become more flattened out at densities above the BG closure. As with our our results for the DC conductivity, the strong increase with the density does not correlate strongly with BG closure and instead correlates more strongly with the conditions where $k_B T$ approaches the value of the BG. The reason for this correlation is most likely due to thermal excitation, see the discussion in Sec. III C.

Our low-density reflectivity trends reproduce the results of Refs. [33,80] as well as the results of Ref. [35] within the error bars. Similar to the discussion of Fig. 3 the reflectivity at which the BG according to the *histogram* method closes (30% to 40%) is smaller than the DC conductivity at which the BG according to the *HOMO-LUMO* closes in Ref. [35] (45% to 60%). In Ref. [35], the reflectivity at the BG closure increases systematically with decreasing density, from 45% at 24 g/cm^3 over 55% at 15 g/cm^3 to somewhere below 60% at 7 g/cm^3 , while our corresponding results fluctuate between 33% and 41%.

E. Ionization

We utilize the TRK sum rule method and the DOS integration approach as discussed in Sec. II E to calculate the ionization degree α via Eq. (8). Results are shown in Fig. 5.

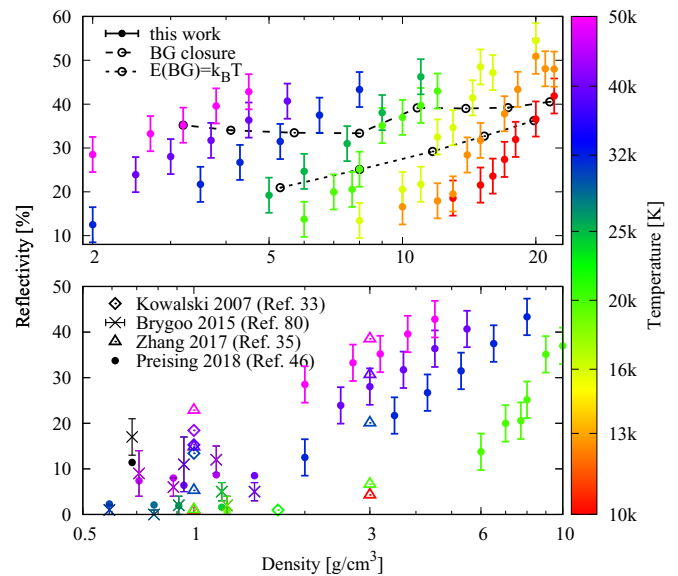


FIG. 4. Reflectivity at 532 nm as a function of density for different isotherms (color-coded). Note that the highest temperature of Ref. [80] is greater than the highest temperature considered here. For the sake of completeness, we added the corresponding data in black. The upper panel shows the results of this work: filled circles are our reflectivity results, open black symbols along the dashed line denote the interpolated reflectivity at which the BG according to the *histogram* method closes. Open black symbols along the dotted line show the interpolated reflectivity at which the BG equals $k_B T$. The lower panel compares the reflectivity of selected isotherms with the results of Refs. [33,35,46,80], denoted as open diamonds, crosses, upper triangles, and filled circles without error bars, respectively.

Consistent with our previous results, the ionization degree obtained via the TRK sum rule method shows pressure ionization, i.e., a significant increase from below 10% at 2 g/cm^3 to more than 99% at the highest densities. The exact values seem to be virtually independent of temperature within our error bars and mostly depend on density. The interpolated α

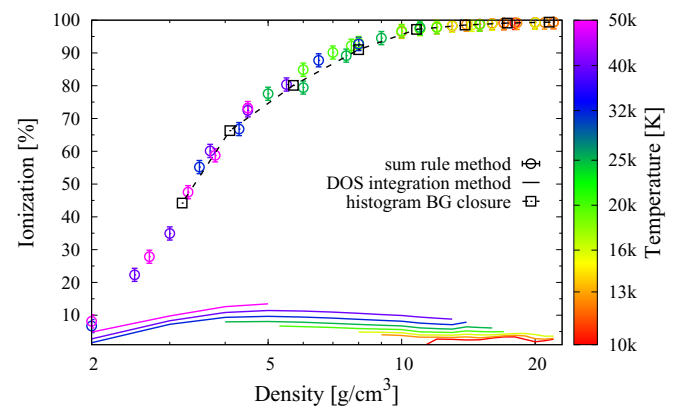


FIG. 5. Ionization degree α as a function of density at different isotherms (color-coded). Open circles with error bars show the results of the TRK sum rule method, while solid lines denote the results of the DOS integration method. Open black symbols along the dashed line show the interpolated α values at which the BG closes according to the *histogram* approach.

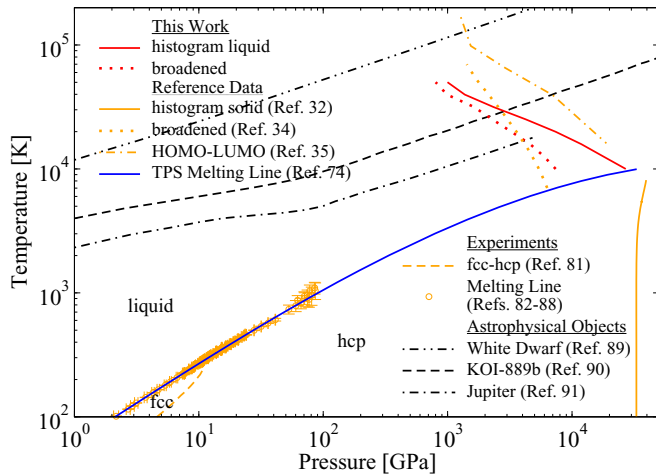


FIG. 6. Phase diagram of helium in the temperature-pressure plane: the melting line from *ab initio* simulations of Preising *et al.* [74] (bold blue line) and experimental data (dashed orange line and symbols) of Refs. [81–88]. Shown are the P - T conditions where the BG closes in fluid helium according to the *broadened* method (dotted lines, results of Ref. [34] in orange and of this work in red), the *histogram* technique of this work for the fluid (bold red line) and that of Ref. [32] for the solid (bold orange line), and the *HOMO-LUMO* definition of Ref. [35] (orange dash-dotted line). The black lines display exemplarily P - T conditions for astrophysical objects which contain substantial fractions of helium: an old white dwarf [89], the brown dwarf KOI-889b [90], and the gas giant planet Jupiter [91].

at which the BG closes according to the *histogram* technique therefore closely resembles the course of α over the density. In contrast, the results of the DOS integration approach are more temperature-dependent. The most striking result in this context is that the DOS integration method fails to show pressure ionization: the ionization degree is less than 15% for all considered densities and temperatures. Actually, the ionization seems to decrease slightly at the highest densities. We therefore conclude that the DOS integration method is not at all suited for the description of pressure ionization, at least in high-density fluid helium.

Note that the ionization degree derived from the TRK sum rule confirms the general trends predicted by chemical models, see, e.g., Ref. [26]: low ionization degree at low densities though increasing with temperature, full ionization at high densities. Note that we do not find any evidence for an instability region (PPT) inbetween as characteristic of chemical models.

F. High-pressure phase diagram of helium

Our results of neither the EOS, the DC conductivity, the reflectivity or the ionization degree demonstrate hints where the nonmetal-to-metal phase transition takes place. We instead use the *histogram* BG closure as a marker for the IMT. We summarize our findings for the IMT in dense fluid helium and propose a new high-pressure phase diagram in Fig. 6, with special emphasis on the region where the BG closes.

We consider the *histogram* method as most reliable in order to locate the BG closure and the corresponding IMT in dense fluid helium in P - T space. Therefore, the bold red line in

Fig. 6 separates the nonmetallic (left) from the metallic fluid (right) according to our extensive DFT-MD simulations and evaluations outlined in detail in Secs. III A to III E.

The IMT in solid helium from the *histogram* method in Ref. [32] intersects the melting line of Ref. [74] at a few tens of terapascals. Disorder as well as the movement of the atoms shift the metallization transition in the fluid toward lower pressures. Therefore our result for the IMT in the fluid with the *histogram* approach is consistent with the corresponding IMT of Ref. [32] in the solid. This agreement further increases our confidence in the *histogram* technique for the prediction of reliable BGs.

According to the *broadened* method, the BG closure occurs at lower densities than predicted by the *histogram* approach. This is expected as the BG of the *broadened* technique is smaller than that of the *histogram* method at high densities, see Fig. 2 and Ref. [54]. At lower pressures, however, the pressure difference between the BG closure as predicted by the two methods decreases.

Our result derived from the *broadened* approach (dotted lines) is quite similar to that of Ref. [34]. The origin of the different slopes for the BG closure curves is most likely due to the use of different XC functionals and numbers of atoms. We used PBE and at least 128 atoms, while Ref. [34] used PW91 and 64 atoms.

The BG closure according to the *histogram* method is located between the *HOMO-LUMO* results of Ref. [35] and our results using the *broadened* approach. This behavior is expected and reproduces the trends shown in Fig. 2.

Based on our results, we can infer consequences for the interior composition of astrophysical objects like gas giant planets, brown dwarfs, or the atmosphere of old and cool white dwarfs which contain large fractions of helium. For instance, the P - T conditions inside Jupiter [91], the largest gas giant planet in our Solar System, do not intersect our results for BG closure according to the *histogram* method (bold red line in Fig. 6) which we consider as most reliable. Therefore Jupiter probably does not contain metallic helium in its deep interior. Since hydrogen is metallic under these conditions [5,71], the consequences for H-He demixing, the solubility of heavier elements in H-He (core erosion), and its actual structure near the core have to be studied, see Refs. [7,92] for recent surveys. However, extrasolar gas giant planets that are larger and hotter than Jupiter (hot Jupiters) [93] reach more extreme P - T conditions in their interior and could, therefore, contain metallic helium. This has consequences for the calculation of their interior profiles, evolution scenarios, and magnetic field structure [3]. The brown dwarf KOI-889b intersects the metallization lines of all methods shown in Fig. 6 and therefore probably contains metallic helium in its deep interior. The representative white dwarf model [89] has a higher temperature than the scope of this study. However, unless the slope of the band gap closure lines changes drastically, this particular white dwarf should contain metallic helium.

The higher-order nature of the nonmetal-to-metal phase transition in dense fluid helium results in a continuous behavior of all properties under study. Around the *histogram* BG closure the DC conductivity fluctuates around 0.4×10^6 S/m, the reflectivity is within 30 to 40%, and the ionization degree

increases continuously from below 10% at the lowest density to more than 99% at the highest densities.

IV. CONCLUSION

We simulated dense fluid helium with DFT-MD simulations in order to investigate the metallization transition in detail. We were especially interested whether the metallization leads to a first-order phase transition as predicted earlier [26,27]. Hence, we calculated the EOS, the BG closure with different methods, the DC conductivity, the optical reflectivity, and the ionization degree from the DFT-MD simulations for a wide range of densities and temperatures. We found no indications for jumps or discontinuities in any of our results. In particular, the ionization calculated from the TRK sum rule method clearly shows a continuous transition to full ionization of 2.0, see Fig. 5. Therefore, we conclude that the metallization transition in dense fluid helium is driven by BG closure and continuous or of higher order, see Fig. 6.

The conventional DOS integration method for the calculation of the ionization degree did not capture pressure

ionization, contrary to the TRK sum rule method. We therefore recommend to use the TRK sum rule method for the calculation of the ionization degree in high-density plasmas where pressure ionization is significant.

In a future study, we will investigate whether the DC conductivity, the reflectivity, and the ionization degree obtained from the TRK sum rule can reproduce temperature ionization at densities below the scope of this study. It is known that the DOS integration method describes temperature ionization reasonably well, in contrast to the pressure ionization that we investigated in this study. We will also employ different XC functionals in order to study their influence on the evolution of the BG.

ACKNOWLEDGMENTS

We thank M. French, C. Kellermann, L. Stixrude, M. Schöttler, M. Bethkenhagen, and M. Schörner for helpful discussions. This work was supported by the North German Supercomputing Alliance (HLRN) and the ITMZ of the University of Rostock as well as by the Deutsche Forschungsgemeinschaft (DFG) via the Research Unit FOR 2440.

-
- [1] K. A. Olive, G. Steigman, and T. P. Walker, *Phys. Rep.* **333-334**, 389 (2000).
- [2] E. G. Adelberger, A. Garcia, R. G. Robertson, K. A. Snover, A. B. Balantekin, K. Heeger, M. J. Ramsey-Musolf, D. Bemmerer, A. Junghans, C. A. Bertulani, J. W. Chen, H. Costantini, P. Prati, M. Couder, E. Uberseder, M. Wiescher, R. Cyburt, B. Davids, S. J. Freedman, M. Gai, D. Gazit, L. Gialanella, G. Imbriani, U. Greife, M. Hass, W. C. Haxton, T. Itahashi, K. Kubodera, K. Langanke, D. Leitner, M. Leitner, P. Vetter, L. Winslow, L. E. Marcucci, T. Motobayashi, A. Mukhamedzhanov, R. E. Tribble, K. M. Nollett, F. M. Nunes, T. S. Park, P. D. Parker, R. Schiavilla, E. C. Simpson, C. Spitaleri, F. Strieder, H. P. Trautvetter, K. Suemmerer, and S. Typel, *Rev. Mod. Phys.* **83**, 195 (2011).
- [3] T. Gastine, J. Wicht, L. D. V. Duarte, M. Heimpel, and A. Becker, *Geophys. Res. Lett.* **41**, 5410 (2014).
- [4] H.-k. Mao and R. J. Hemley, *Rev. Mod. Phys.* **66**, 671 (1994).
- [5] J. M. McMahon, M. A. Morales, C. Pierleoni, and D. M. Ceperley, *Rev. Mod. Phys.* **84**, 1607 (2012).
- [6] A. Goncharov, *Low Temp. Phys.* **46**, 97 (2020).
- [7] R. Helled, G. Mazzola, and R. Redmer, *Nat. Rev. Phys.* **2**, 562 (2020).
- [8] K. F. Herzfeld, *Phys. Rev.* **29**, 701 (1927).
- [9] N. F. Mott, *Proc. Phys. Soc. A* **62**, 416 (1949).
- [10] P. P. Edwards, M. T. J. Lodge, F. Hensel, and R. Redmer, *Philos. Trans. R. Soc. A* **368**, 941 (2010).
- [11] E. Wigner and H. B. Huntington, *J. Chem. Phys.* **3**, 764 (1935).
- [12] P. Loubeyre, F. Occelli, and P. Dumas, *Nature (London)* **577**, 631 (2020).
- [13] S. T. Weir, A. C. Mitchell, and W. J. Nellis, *Phys. Rev. Lett.* **76**, 1860 (1996).
- [14] M. D. Knudson, M. P. Desjarlais, A. Becker, R. W. Lemke, K. R. Cochrane, M. E. Savage, D. E. Bliss, T. R. Mattsson, and R. Redmer, *Science* **348**, 1455 (2015).
- [15] P. M. Celliers, M. Millot, S. Brygoo, R. S. McWilliams, D. E. Fratanduono, J. R. Rygg, A. F. Goncharov, P. Loubeyre, J. H. Eggert, J. L. Peterson, N. B. Meezan, S. Le Pape, G. W. Collins, R. Jeanloz, and R. J. Hemley, *Science* **361**, 677 (2018).
- [16] M. P. Desjarlais, M. D. Knudson, and R. Redmer, *Phys. Rev. B* **101**, 104101 (2020).
- [17] H. Y. Geng, Q. Wu, M. Marqués, and G. J. Ackland, *Phys. Rev. B* **100**, 134109 (2019).
- [18] V. Y. Ternovoi, A. S. Filimonov, A. A. Pyalling, V. B. Mintsev, and V. E. Fortov, *AIP Conf. Proc.*, **620**, 107 (2002).
- [19] A. Kietzmann, B. Holst, R. Redmer, M. P. Desjarlais, and T. R. Mattsson, *Phys. Rev. Lett.* **98**, 190602 (2007).
- [20] P. M. Celliers, P. Loubeyre, J. H. Eggert, S. Brygoo, R. S. McWilliams, D. G. Hicks, T. R. Boehly, R. Jeanloz, and G. W. Collins, *Phys. Rev. Lett.* **104**, 184503 (2010).
- [21] V. Fortov, *Thermodynamics and Equations of State for Matter* (World Scientific, Singapore, 2016).
- [22] C. A. T. Seldam, *Proc. Phys. Soc. Sect. A* **70**, 97 (1957).
- [23] L. N. Simcox and N. H. March, *Proc. Phys. Soc.* **80**, 830 (1962).
- [24] D. Brust, *Phys. Lett. A* **40**, 255 (1972).
- [25] D. A. Young, A. K. McMahan, and M. Ross, *Phys. Rev. B* **24**, 5119 (1981).
- [26] A. Förster, T. Kahlbaum, and W. Ebeling, *Laser Part. Beams* **10**, 253 (1992).
- [27] T. Kahlbaum and A. Förster, *Fluid Phase Equilib.* **76**, 71 (1992).
- [28] D. Saumon, G. Chabrier, and H. M. van Horn, *Astrophys. J. Suppl. Ser.* **99**, 713 (1995).
- [29] C. Winisdoerffer and G. Chabrier, *Phys. Rev. E* **71**, 026402 (2005).
- [30] S. A. Khairallah and B. Militzer, *Phys. Rev. Lett.* **101**, 106407 (2008).
- [31] L. Landau and J. Zeldovich, *Acta Physicochim. USSR* **18**, 194 (1943).

- [32] B. Monserrat, N. D. Drummond, C. J. Pickard, and R. J. Needs, *Phys. Rev. Lett.* **112**, 055504 (2014).
- [33] P. M. Kowalski, S. Mazevet, D. Saumon, and M. Challacombe, *Phys. Rev. B* **76**, 075112 (2007).
- [34] L. Stixrude and R. Jeanloz, *Proc. Natl. Acad. Sci. U.S.A.* **105**, 11071 (2008).
- [35] W. Zhang, Z. Li, Z. Fu, J. Dai, Q. Chen, and L. Cai, *Sci. Rep.* **7**, 41885 (2017).
- [36] J. Eggert, S. Brygoo, P. Loubeyre, R. S. McWilliams, P. M. Celliers, D. G. Hicks, T. R. Boehly, R. Jeanloz, and G. W. Collins, *Phys. Rev. Lett.* **100**, 124503 (2008).
- [37] R. S. McWilliams, D. A. Dalton, Z. Konôpková, M. F. Mahmood, and A. F. Goncharov, *Proc. Natl. Acad. Sci.* **112**, 7925 (2015).
- [38] M. Bethkenhagen, B. B. L. Witte, M. Schörner, G. Röpke, T. Döppner, D. Kraus, S. H. Glenzer, P. A. Sterne, and R. Redmer, *Phys. Rev. Research* **2**, 023260 (2020).
- [39] P. Hohenberg and W. Kohn, *Phys. Rev.* **136**, B864 (1964).
- [40] W. Kohn and L. J. Sham, *Phys. Rev.* **140**, A1133 (1965).
- [41] G. Kresse and J. Hafner, *Phys. Rev. B* **47**, 558 (1993).
- [42] G. Kresse and J. Hafner, *Phys. Rev. B* **49**, 14251 (1994).
- [43] G. Kresse and J. Furthmüller, *Phys. Rev. B* **54**, 11169 (1996).
- [44] G. Kresse and J. Furthmüller, *Comput. Mater. Sci.* **6**, 15 (1996).
- [45] J. Hafner, *J. Comput. Chem.* **29**, 2044 (2008).
- [46] M. Preising, W. Lorenzen, A. Becker, R. Redmer, M. D. Knudson, and M. P. Desjarlais, *Phys. Plasmas* **25**, 012706 (2018).
- [47] S. Nosé, *J. Chem. Phys.* **81**, 511 (1984).
- [48] S. Nosé, *Prog. Theor. Phys. Suppl.* **103**, 1 (1991).
- [49] D. M. Bylander and L. Kleinman, *Phys. Rev. B* **46**, 13756 (1992).
- [50] A. Baldereschi, *Phys. Rev. B* **7**, 5212 (1973).
- [51] H. J. Monkhorst and J. D. Pack, *Phys. Rev. B* **13**, 5188 (1976).
- [52] J. P. Perdew, K. Burke, and M. Ernzerhof, *Phys. Rev. Lett.* **77**, 3865 (1996).
- [53] P. E. Blöchl, *Phys. Rev. B* **50**, 17953 (1994).
- [54] See Supplemental Material at <http://link.aps.org/supplemental/10.1103/PhysRevB.102.224107> for an in-depth discussion of the calculation of the ionization degree, the band gap approaches and their convergence as well as the convergence of the EOS, the DC conductivity, the reflectivity, and the ionization degree.
- [55] F. Soubiran, S. Mazevet, C. Winisdoerffer, and G. Chabrier, *Phys. Rev. B* **86**, 115102 (2012).
- [56] R. Kubo, *J. Phys. Soc. Jpn.* **12**, 570 (1957).
- [57] D. A. Greenwood, *Proc. Phys. Soc.* **71**, 585 (1958).
- [58] M. Gajdoš, K. Hummer, G. Kresse, J. Furthmüller, and F. Bechstedt, *Phys. Rev. B* **73**, 045112 (2006).
- [59] B. Holst, M. French, and R. Redmer, *Phys. Rev. B* **83**, 235120 (2011).
- [60] M. French and R. Redmer, *Phys. Plasmas* **24**, 092306 (2017).
- [61] D. B. Melrose and R. C. McPhedran, *Electromagnetic Processes in Dispersive Media* (Cambridge University Press, Cambridge, 1991).
- [62] S. Mazevet, J. D. Kress, L. A. Collins, and P. Blottiau, *Phys. Rev. B* **67**, 054201 (2003).
- [63] S. Mazevet, M. P. Desjarlais, L. A. Collins, J. D. Kress, and N. H. Magee, *Phys. Rev. E* **71**, 016409 (2005).
- [64] S. M. Vinko, O. Ciricosta, and J. S. Wark, *Nat. Commun.* **5**, 3533 (2014).
- [65] S. X. Hu, *Phys. Rev. Lett.* **119**, 065001 (2017).
- [66] K. P. Driver, F. Soubiran, and B. Militzer, *Phys. Rev. E* **97**, 063207 (2018).
- [67] W. Thomas, *Naturwissenschaften* **13**, 627 (1925).
- [68] F. Reiche and W. Thomas, *Z. Phys.* **34**, 510 (1925).
- [69] W. Kuhn, *Z. Phys.* **33**, 408 (1925).
- [70] M. P. Desjarlais, J. D. Kress, and L. A. Collins, *Phys. Rev. E* **66**, 025401(R) (2002).
- [71] W. Lorenzen, B. Holst, and R. Redmer, *Phys. Rev. B* **82**, 195107 (2010).
- [72] W. Lorenzen, B. Holst, and R. Redmer, *Phys. Rev. B* **84**, 235109 (2011).
- [73] M. A. Morales, C. Pierleoni, E. Schwegler, and D. M. Ceperley, *Proc. Natl. Acad. Sci. U.S.A.* **107**, 12799 (2010).
- [74] M. Preising and R. Redmer, *Phys. Rev. B* **100**, 184107 (2019).
- [75] J. P. Perdew and Y. Wang, *Phys. Rev. B* **45**, 13244 (1992).
- [76] R. Redmer, *Phys. Rev. E* **59**, 1073 (1999).
- [77] S. Kuhlbrodt and R. Redmer, *Phys. Rev. E* **62**, 7191 (2000).
- [78] S. Kuhlbrodt, R. Redmer, H. Reinholz, G. Röpke, B. Holst, V. B. Mintsev, V. K. Gryaznov, N. S. Shilkin, and V. E. Fortov, *Contrib. Plasma Phys.* **45**, 61 (2005).
- [79] J. R. Adams, H. Reinholz, R. Redmer, V. B. Mintsev, N. S. Shilkin, and V. K. Gryaznov, *Phys. Rev. E* **76**, 036405 (2007).
- [80] S. Brygoo, M. Millot, P. Loubeyre, A. E. Lazicki, S. Hamel, T. Qi, P. M. Celliers, F. Coppari, J. H. Eggert, D. E. Fratanduono, D. G. Hicks, J. R. Rygg, R. F. Smith, D. C. Swift, G. W. Collins, and R. Jeanloz, *J. Appl. Phys.* **118**, 195901 (2015).
- [81] P. Loubeyre, R. LeToullec, J. P. Pinceaux, H. K. Mao, J. Hu, and R. J. Hemley, *Phys. Rev. Lett.* **71**, 2272 (1993).
- [82] J. S. Dugdale and D. K. C. MacDonald, *Phys. Rev.* **89**, 832 (1953).
- [83] R. K. Crawford and W. B. Daniels, *J. Chem. Phys.* **55**, 5651 (1971).
- [84] R. L. Mills, D. H. Liebenberg, and J. C. Bronson, *Phys. Rev. B* **21**, 5137 (1980).
- [85] P. Loubeyre, J. M. Besson, J. P. Pinceaux, and J. P. Hansen, *Phys. Rev. Lett.* **49**, 1172 (1982).
- [86] W. L. Vos, M. G. E. van Hinsberg, and J. A. Schouten, *Phys. Rev. B* **42**, 6106 (1990).
- [87] F. Datchi, P. Loubeyre, and R. Le Toullec, *Phys. Rev. B* **61**, 6535 (2000).
- [88] D. Santamaría-Pérez, G. D. Mukherjee, B. Schwager, and R. Boehler, *Phys. Rev. B* **81**, 214101 (2010).
- [89] E. Y. Chen and B. M. S. Hansen, *Mon. Not. R. Astron. Soc.* **413**, 2827 (2011).
- [90] A. Becker, M. Bethkenhagen, C. Kellermann, J. Wicht, and R. Redmer, *Astron. J.* **156**, 149 (2018).
- [91] W. B. Hubbard and B. Militzer, *Astrophys. J.* **820**, 80 (2016).
- [92] F. Debras and G. Chabrier, *Astrophys. J.* **872**, 100 (2019).
- [93] D. P. Thorngren and J. J. Fortney, *Astron. J.* **155**, 214 (2018).